Accelerated Publications

X-ray Absorption Spectroscopic Investigation of the Resting Ferrous and Cosubstrate-Bound Active Sites of Phenylalanine Hydroxylase[†]

Erik C. Wasinger,[‡] Nataša Mitić,[‡] Britt Hedman,*,[‡],[§] John Caradonna,*,[‖] Edward I. Solomon,*,[‡] and Keith O. Hodgson*,[‡],[§]

Department of Chemistry, Stanford University, Stanford, California 94305, Stanford Synchrotron Radiation Laboratory, SLAC, Stanford University, Stanford, California 94309, and Department of Chemistry, Boston University, Boston, Massachusetts 02215

Received December 12, 2001; Revised Manuscript Received February 26, 2002

ABSTRACT: Previous studies of ferrous wild-type phenylalanine hydroxylase, ${Fe^{2+}}PAH^T[]$, have shown the active site to be a six-coordinate distorted octahedral site. After the substrate and cofactor bind to the enzyme (${Fe^{2+}}PAH^R[L\text{-Phe},5\text{-deaza-6-MPH}_4]$), the active site converts to a five-coordinate square pyramidal structure in which the identity of the missing ligand had not been previously determined. X-ray absorption spectroscopy (XAS) at the Fe K-edge further supports this coordination number change with the binding of both cosubstrates to the enzyme, and determines this to be due to the loss of a water ligand.

The pterin-dependent hydroxylases, one class of mononuclear non-heme iron proteins (*1*, *2*), perform a variety of critical catalytic functions, including the mediation of proper brain function, regulation of amino acid metabolism, and activation of dioxygen for specific oxygenation reactions (*3*). This class of enzymes, consisting of phenylalanine (PAH)[1] (*4*, *5*), tyrosine (TyrH) (*6*–*8*), and tryptophan (TrpH) (*9*) hydroxylases, perform potentially rate-limiting steps in phenylalanine catabolism (*4*, *5*), epinephrine/catecholamine biosynthesis (*6*–*8*), and serotonin biosynthesis (*9*), respec-

tively. Specifically, PAH initiates the detoxification of high levels of phenylalanine; the proper functioning of PAH is essential in eliminating abnormal accumulation of neurotoxic L-Phe-based metabolic products. Dysfunction of PAH can lead to phenylketonuria, PKU (*10*, *57*), a genetic disorder affecting 1 in 10 000 infants in the United States, resulting in postnatal brain damage and severe, progressive mental retardation.

Rat hepatic PAH (phenylalanine 4-monooxygenase, EC 1.14.16.1) is the most widely studied of the pterin-dependent hydroxylases due to its abundance, solubility, and ease of purification (*3*–*5*). PAH exists as a homodimer or tetramer of 51.7 kDa subunits (*11*, *12*), each of which contains a non-heme iron site required for activity (*13*, *14*). During hy-

[1] Abbreviations: XAS, X-ray absorption spectroscopy; EXAFS, extended X-ray absorption fine structure; TMC, 1,4,8,11-tetramethyl-l,4,8,11-tetraazacyclotetradecane; Im, imidazole; PKU, phenylketonurea; PAH, phenylalanine hydroxylase; TyrH, tyrosine hydroxylase; TrpH, tryptophan hydroxylase; BH$_4$, tetrahydrobiopterin; 6-MPH$_4$, 6-methyltetrahydropterin.
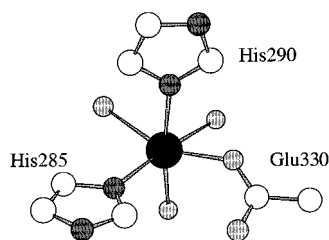
FIGURE 1: Crystal structure active site of truncated ferric PAH used as a starting model for {Fe^{2+}}PAH^T[] and {Fe^{2+}}PAH^R[L-Phe,5-deaza-6-MPH$_4$] in the EXAFS fits. Carbon atoms are shown in white; oxygen atoms are shown with light shading, and nitrogen atoms are shown as dark shaded spheres.

droxylation of L-Phe, PAH uses reduced tetrahydrobiopterin (BH$_4$) cofactor and dioxygen in a coupled mechanism to generate L-Tyr and 4a-hydroxytetrahydropterin (*15*), where dioxygen is partitioned between the phenolic hydroxyl group of tyrosine and the oxidized pterin. The oxidized pterin is recycled back to BH$_4$ via 4a-carbinolamine dehydratase (DcoH) and dihydropteridine reductase (DHPR). PAH is highly regulated by both its natural substrate L-Phe and cofactor BH$_4$ that serve to activate and reduce the enzyme. Prior to becoming catalytically competent, PAH must be allosterically activated by L-Phe and reduced by BH$_4$ (*4, 16–22*). Addition of L-Phe to the resting low-affinity "tense" state Fe^{2+}PAH^T[] results in a large structural rearrangement and conversion to the activated high-affinity "relaxed" Fe^{2+}-PAH^R[L-Phe] state. The activation barrier for this interconversion is ~34 kcal/mol (*11*), and it has been shown by earlier studies that allosteric and nonallosteric methods of activation are not associated with any direct change in the iron active site (*23, 24*).

Most studies on PAH to date have focused on the more spectroscopically accessible ferric form of the enzyme (*21, 24, 25*). Crystal structures of the truncated ferric form of the enzyme (Figure 1) have been determined (*26–29*) and confirm earlier studies reporting His285 and His290 as ligands to the active site iron (*30*). Monodentate Glu330 and three water molecules complete the active site ligation (*31*). In the active form of the enzyme, however, the active site contains a ferrous center, and few studies (*23, 32, 33*), including a recent crystal structure (*34*), have related to this reduced site. It should be noted, however, that additional studies have been performed utilizing pulsed EPR methods (*35*) on the {FeNO}^{7} adduct, in which NO binds to Fe(II)−PAH to produce the Fe^{3+}−NO$^-$ species (*36*). Defining the electronic and geometric structure of the active site in the reduced form of the enzyme is essential to understanding the role it plays in the catalytic mechanism of PAH. Our previous CD, MCD, and XAS studies have shown {Fe^{2+}}-PAH^T[] to be a distorted six-coordinate site, and that addition of the substrate and cofactor analogue to the protein to form {Fe^{2+}}PAH^R[L-Phe,5-deaza-6-MPH$_4$] results in a five-coordinate active site; the identity of the ligand that is lost, however, could not be determined (*23, 33*).

Using X-ray absorption spectroscopy, we have investigated the changes at the active site that accompany the conversion of PAH in the tense state to the resting state using L-Phe and the redox inactive pterin analogue, 5-deaza-6-methyltetrahydropterin (5-deaza-6-MPH$_4$) (*24, 37*). This approach simplifies the preparative aspects (compared to using redox

active pterins) while effectively probing active site structural changes associated with inhibition and regulation of the enzyme. The crystal structure, although not of the active form of PAH, serves as a geometric starting model for {Fe^{2+}}-PAH^T[] (Figure 1) and has been extended to {Fe^{2+}}-PAH^R[L-Phe,5-deaza-6-MPH$_4$] by sequentially fitting EXAFS data assuming the loss of a histidine, glutamate, or water ligand. These results extend earlier CD and MCD studies and identify the ligand lost at the Fe(II) active site of PAH, due to the binding of the substrate and cofactor, as water.

MATERIALS AND METHODS

The cofactor analogue 5-deaza-6-MPH$_4$ was synthesized (*37–39*), and the PAH enzyme was isolated following modified literature procedures (*33*) for use in anaerobically preparing {Fe^{2+}}PAH^T[] and {Fe^{2+}}PAH^R[L-Phe,5-deaza-6-MPH$_4$] as previously described (*33*). To facilitate glass formation for XAS studies, the concentrated aqueous protein solutions were diluted with 55−65% (v:v) glycerol in buffer, resulting in final sample concentrations of 2.0 and 1.6 mM for {Fe^{2+}}PAH^T[] and {Fe^{2+}}PAH^R[L-Phe,5-deaza-6-MPH$_4$], respectively. The enzymatic activity was 6.8 units/mg for both samples before XAS experiments. Samples were frozen at −80 °C until further use. The presence of glycerol as a glassing agent and low temperature have previously been confirmed to have no effect on the ferrous active site of PAH via CD and MCD spectroscopies (*23*). For each sample, approximately 100 μL of an anaerobically thawed sample solution was transferred into a 23 mm × 1 mm × 3 mm Lucite XAS cell with 37 μm Kapton windows and immediately frozen in liquid nitrogen.

For XAS edge comparisons to {Fe^{2+}}PAH^T[] and {Fe^{2+}}-PAH^R[L-Phe,5-deaza-6-MPH$_4$], [Fe(Im)$_6$]Cl$_2$ and [Fe(TMC)-Cl](BF$_4$)$_2$ were used as six- and five-coordinate ferrous models, respectively. The crystalline models were mixed with boron nitride (BN) and ground to a fine powder. The sample mixture was pressed into a 1 mm thick aluminum spacer sealed with Kapton windows.

X-ray absorption spectra were recorded at the Stanford Synchrotron Radiation Laboratory (SSRL) on beam line 9-3 under standard conditions of 3 GeV and 50−100 mA. The beam line utilizes a Rh-coated harmonic rejection and collimation mirror, set to a cutoff of 11 keV, a Si(220) double-crystal monochromator (fully tuned), and a cylindrical bent focusing Rh-coated mirror. Data were obtained to $k = 15$ Å^{-1} with 1 mm high in-hutch slits. A constant sample temperature of 10 K was maintained using an Oxford Instruments liquid helium CF1208 cryostat. Each scan was internally calibrated using an iron foil, assigning the first inflection point to 7111.2 eV (*40*). The spectrometer energy resolution was better than 1.4 eV with reproducibility in the edge position of <0.2 eV. The Fe Kα fluorescence data were measured using a 30-element Ge solid-state array detector (*41*) with a three-wavelength Mn filter and Soller slits aligned between the detector and the sample to improve the ratio of useable Fe Kα fluorescence signal to that of the scattered beam. Data were monitored for sample integrity by averaging sets of four successive scans and comparing a four-scan average to the previous averages. In this manner, no change in the edge or EXAFS regions was observed; thus, all scans of a given sample could be used for a final, averaged data set.

For {Fe^{2+}}PAH^T[] and {Fe^{2+}}PAH^R[L-Phe,5-deaza-6-MPH$_4$], 26 and 35 scans, respectively, were obtained and averaged to reduce the noise level of the data. Reduction and normalization of the averaged data were performed according to established methods (*42–44*). A smooth pre-edge Gaussian background function modeling the elastically scattered beam was removed from the spectra. For each sample, a three-segment spline through the EXAFS region approximately equal in *k* space was chosen, and each sample was normalized to an edge jump of 1.0 at 7130 eV. Further explanation of data reduction, background subtraction, and normalization procedures can be found in ref *45* and references therein.

The intensities and energies of the pre-edge features of all samples were quantified using the fitting program EDG_FIT (*46*). All spectra were fit over the range of 7106–7118 eV, modeling the pre-edge features with pseudo-Voigt line shapes of a fixed 1:1 ratio of Lorentzian to Gaussian contributions. Functions modeling the background were chosen empirically to give the best fit while simultaneously reproducing shoulders on the rising edge. A fit was considered acceptable only if it successfully reproduced the data and the second derivative of the data over the entire fit range. For all complexes, 8–10 successful fits were obtained that reproduced the data and second derivative while varying the background function used between fits. The total pre-edge area is the sum of the areas of all pre-edge features for a sample, where the pre-edge area for a feature is approximated by peak height multiplied by the full width at half maximum scaled by 100. To quantify the error, standard deviations for peak heights and half-widths were calculated for each pre-edge feature from all successful fits of a sample.

Theoretical EXAFS signals, $\chi(k)$, were calculated using FEFF (version 6) and the crystal structure (Figure 1) (*31*) as a starting model. The model was fit to the EXAFS data using EXAFSPAK (written by G. N. George, SSRL). The structural parameters R, the bond distance in angstroms, and σ^2, the bond variance in square angstroms, were varied in the fits of each sample. The bond variance is related to the Debye–Waller factor, a measure of the thermal vibration of the absorber–scatterer pair, as well as static disorder. The threshold energy in electronvolts ($k = 0$, E_0) was kept to a common, variable (ΔE_0) value relative to 7130 eV for all components within a given fit of a sample. Fits were evaluated by comparing the normalized error for each fit, F, and by visual inspection of the fits to the EXAFS data and the respective Fourier transforms. Although the first coordination spheres for the PAH samples do not solely have nitrogen ligation, distinguishing between nitrogen and oxygen backscatterers is not possible; therefore, all first-coordination sphere components were fit with nitrogen phases and amplitudes. More distant second-shell single-scattering and multiple-scattering waves were fit with carbon components from FEFF. For preliminary fitting, outer shell single- and multiple-scattering paths were linked together at input model distances with the respective first-coordination sphere component. Debye–Waller factors were set to initial values of 0.00500 Å^2 and allowed to float in all fits. In the final fits, the distance link was released and all components were allowed to float. In all cases, the outer shell components moved very little (<0.05 Å) from their linked positions. On the basis of studies of complexes of known structures, the

uncertainties in final distances are within 0.02 Å. The total coordination number was obtained from pre-edge analysis (vida infra); however, the distribution of ligands into shorter or longer components was varied in integer steps to determine the best fit.

RESULTS

Fe K-Edge Analysis. Fe K-edge energy positions are known to be indicative of the oxidation state of the material. Edges of reduced complexes are shifted to lower energy relative to their oxidized counterparts because of the increased level of charge donation to the metal site. Furthermore, model studies have shown that the intensity patterns of pre-edge spectra of Fe^{II} complexes are a significant diagnostic tool, which can directly correlate edge structure to site coordination and geometry (*47, 48*). The 1s → 3d transition is electric dipole-forbidden; thus, for centrosymmetric complexes, the pre-edge intensity derives from the ∼100-fold weaker electric quadrupole transition mechanism. Ferrous six-coordinate complexes have pre-edges which typically have a total normalized area of ∼4 units and are comprised of three features. Ligand field analysis predicts three allowed transitions separated by ∼0.9 and ∼1.3 eV, respectively. Since the resolution at the Fe K-edge is on the order of 1.4 eV, the first two transitions overlap; thus, the middle band typically can be resolved as a high-energy shoulder on the lowest-energy feature (*48*). The center of inversion is eliminated in five- and four-coordinate complexes, typically allowing a few percent 4p orbital mixing into the 3d orbitals. This leads to significant increases in pre-edge intensities in noncentrosymmetric complexes from the electric dipole-allowed 1s → 4p contribution. Thus, five-coordinate C_{4v} ferrous model complex pre-edges have a total area of ∼12 units, and are composed of a relatively intense, lower-energy feature and a relatively weak, higher-energy feature; four-coordinate nonplanar ferrous model complexes have two relatively strong pre-edge features and a total pre-edge area of ∼13 units (*48*). While the intensities of the five- and four-coordinate noncentrosymmetric complexes are similarly large, the sites are differentiated by their respective intensity distributions.

The pre-edge spectra and second derivatives of {Fe^{2+}}-PAH^T[] and {Fe^{2+}}PAH^R[L-Phe,5-deaza-6-MPH$_4$] are shown in Figure 2 along with those of six- and five-coordinate ferrous model compounds. The pre-edge of {Fe^{2+}}PAH^T[] is clearly comprised of three transitions, the lowest-energy peak appearing as a double-well feature in the second derivative (arrows in Figure 2). As described above, this parallels the general shape and intensity pattern for six-coordinate ferrous model complexes. The pre-edge of {Fe^{2+}}-PAH^R[L-Phe,5-deaza-6-MPH$_4$] differs significantly from that of {Fe^{2+}}PAHT[], having only two distinct peaks in the data and second derivative, more resembling the pre-edge of the five-coordinate model compound.

The individual peak energies and the total pre-edge area for both samples are listed in Table 1 along with those of typical five- and six-coordinate model complexes. The total pre-edge area for {Fe^{2+}}PAH^T[] of 8.1 units is greater than that of typical six-coordinate model complexes, but significantly less than that of five-coordinate models. Deviations from a strict octahedral field in protein active sites due to
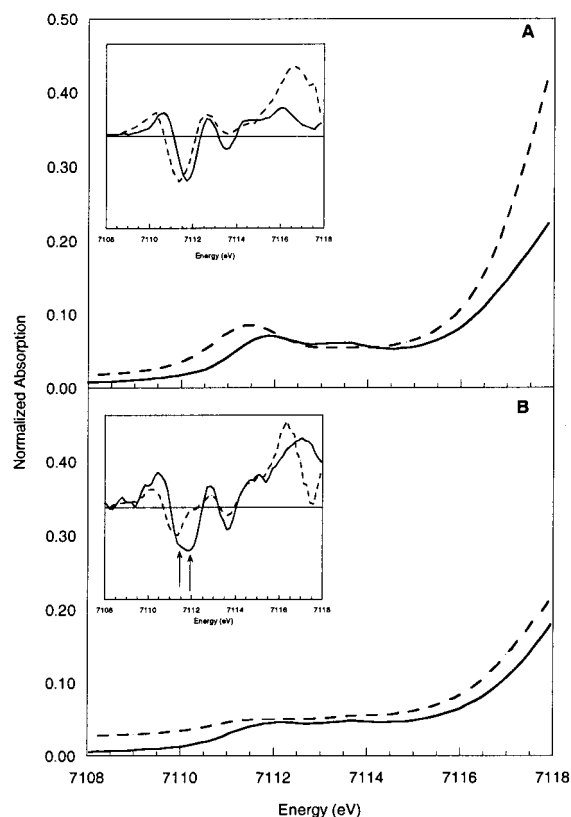
FIGURE 2: (A) Pre-edge spectra of $\{Fe^{2+}\}PAH^R[L\text{-Phe},5\text{-deaza-6-}MPH_4]$ (—) and the five-coordinate model complex $[Fe(TMC)Cl]$-Cl (- - -). (B) Pre-edge spectra of $\{Fe^{2+}\}PAH^T[]$ (—) and the six-coordinate model complex $[Fe(Im_6)]Cl_2$ (- - -). Insets show the second derivatives of the spectra, with the same line designations as for the full spectra.
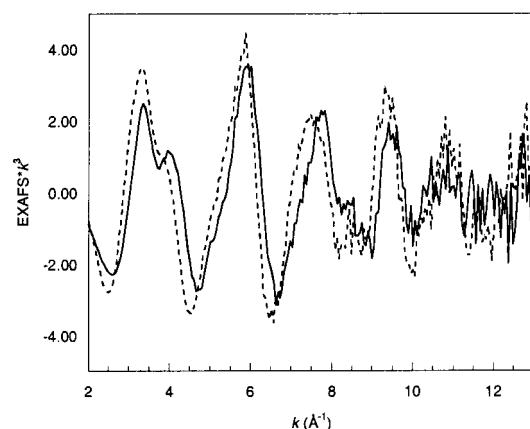

FIGURE 3: EXAFS spectra of $\{Fe^{2+}\}PAH^T[]$ (- - -) and $\{Fe^{2+}\}$-$PAH^R[L\text{-Phe},5\text{-deaza-6-}MPH_4]$ (—).

variations in bond distances, bond angles, and the orbital character of the ligands can promote 4p mixing into the d orbitals, and typically give rise to pre-edge areas greater than those for octahedral model complexes (23, 49, 50). The total pre-edge area for $\{Fe^{2+}\}PAH^R[L\text{-Phe},5\text{-deaza-6-}MPH_4]$ of 13.9 units is similar to that of the square pyramidal model complex. As described in the literature (48), the additional pre-edge intensity of a five-coordinate complex occurs through $4p_z$ mixing into the d_{z^2} orbital in a square pyramidal symmetry.

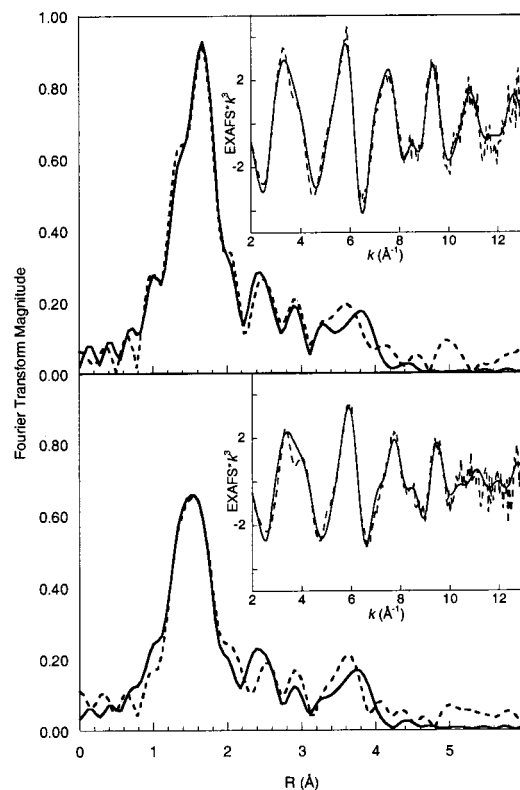*EXAFS Analysis.* The EXAFS data were measured to $k = 15$ Å^{-1}; however, the fits to the data were limited to the

FIGURE 4: Fourier transforms (- - -) and fits (—) to the $\{Fe^{2+}\}$-$PAH^T[]$ (top, Table 2, fit 2) and $\{Fe^{2+}\}PAH^R[L\text{-Phe},5\text{-deaza-6-}MPH_4]$ (bottom, Table 2, fit 5) data. Insets show EXAFS data (- - -) and fits to the EXAFS data (—) of the respective samples.

Table 1: Pre-Edge Features of $\{Fe^{2+}\}PAH^T[]$, $\{Fe^{2+}\}PAH^R[L\text{-Phe},5\text{-deaza-6-}MPH_4]$, and Related Model Complexes

sample[a]	pre-edge peak energy[b]	total area[c]
PAH^T	7111.4(0.0)	8.1(0.4)
	7112.2(0.0)	
	7113.6(0.0)	
PAH^R	7111.7(0.0)	13.9(0.8)
	7113.5(0.1)	
$[Fe(Im)_6]Cl_2$	7111.2(0.0)	3.8(0.3)
	7112.4(0.2)	
	7113.7(0.0)	
$[Fe(TMC)Cl]Cl$	7111.4(0.0)	12.9(0.2)
	7113.4(0.0)	

[a] PAH^T is $\{Fe^{2+}\}PAH^T[]$ and PAH^R $\{Fe^{2+}\}PAH^R[L\text{-Phe},5\text{-deaza-6-}MPH_4]$. [b] Values in parentheses are the statistical standard deviations calculated from the individual acceptable fits used in the analysis. Standard deviations of less than 0.05 eV are rounded to 0.0 eV. [c] The reported values are multiplied by 100 for convenience.

range $k = 2.0-13.0$ Å^{-1} according to the quality of the data averages. The data clearly show differences in the overall EXAFS phase and amplitude (Figure 3). The data for $\{Fe^{2+}\}$-$PAH^R[L\text{-Phe},5\text{-deaza-6-}MPH_4]$ are shifted to higher k space, indicating a shorter average distance, and are lower in amplitude than the EXAFS data for $Fe^{2+}PAH^T[]$. This is also clearly seen in the Fourier transforms of the data (Figure 4), for which the primary disparity between $\{Fe^{2+}\}PAH^T[]$ and $\{Fe^{2+}\}PAH^R[L\text{-Phe},5\text{-deaza-6-}MPH_4]$ is an almost 20% greater intensity in the first-coordination sphere Fourier transform peak for $\{Fe^{2+}\}PAH^T[]$. These differences can be understood in the context of the fits to the EXAFS data described below.

Table 2: EXAFS Fits of $\{Fe^{2+}\}PAH^T[]$ and $\{Fe^{2+}\}PAH^R[L\text{-}Phe,5\text{-}deaza\text{-}6\text{-}MPH_4]$

| | $\{Fe^{2+}\}PAH^T[]$ | | | | | | | | | $\{Fe^{2+}\}PAH^R[L\text{-}Phe,5\text{-}deaza\text{-}6\text{-}MPH_4]$ | | | | | | | | | | | |
| | fit 1 ($E_0 = -2.6$) | | | fit 2 ($E_0 = -3.7$) | | | fit 3 ($E_0 = -4.1$) | | | fit 4 ($E_0 = -3.5$) | | | fit 5 ($E_0 = -4.2$) | | | fit 6 ($E_0 = -4.6$) | | | fit 7 ($E_0 = -3.7$) | | |
	CN	R (Å)	σ^2 (Å²)[a]	CN	R (Å)	σ^2 (Å²)[a]	CN	R (Å)	σ^2 (Å²)[a]	CN	R (Å)	σ^2 (Å²)[a]	CN	R (Å)	σ^2 (Å²)[a]	CN	R (Å)	σ^2 (Å²)[a]	CN	R (Å)	σ^2 (Å²)[a]
Fe−O/N	0	−	−	1	1.97	427	2	2.02	929	0	−	−	1	1.94	300	2	1.98	625	1	1.94	266
Fe−O/N	6	2.13	749	5	2.14	437	4	2.15	415	5	2.07	964	4	2.10	534	3	2.12	457	4	2.10	520
C_α SS[b]	5	3.09	545	5	3.08	507	5	3.08	535	5	3.07	736	5	3.07	725	5	3.06	784	3	3.07	328
C_β SS[b]	4	4.05	715	4	4.05	759	4	4.05	823	4	4.03	534	4	4.02	536	4	4.03	560	2	4.00	242
C_β MS[b]	8	4.38	432	8	4.36	385	8	4.36	349	8	4.31	600	8	4.30	558	8	4.30	507	4	4.32	052
error[c]		0.267			0.216			0.232			0.267			0.232			0.240			0.228	

[a] All Debye−Waller factors are multiplied by 10^5 for convenience. [b] SS, single scattering; MS, multiple scattering. [c] Error (F) is defined as $F = \sum[(\chi_{exp} - \chi_{obsd})^2 k^6]/\sum(\chi_{exp}^2 k^6)$.

From the pre-edge analysis and from MCD results (*23*), $\{Fe^{2+}\}PAH^T[]$ is six-coordinate; thus, EXAFS fits were restricted to a total first coordination sphere of six ligands. Fits of $\{Fe^{2+}\}PAH^T[]$ using only a single contribution of six nitrogens lead to an average distance of 2.13 Å and a relatively high fit value of 0.267 (Table 2, fit 1). The σ^2 factor for this shell is also reasonably high, and indicative of the existence of a split coordination sphere. A fit of one nitrogen at 1.97 Å and five nitrogens at 2.14 Å results in a significant decrease in the σ^2 factor of the original component, a lower error value of 0.216 (Table 2, fit 2), and a better visual fit to the Fourier transform (Figure 4, top, dashed line). Attempting to model the EXAFS with two short ligands and four longer ligands (2.02 and 2.15 Å, respectively) produces a fit with a lowered F value relative to the unsplit first shell (Table 2, fit 3) but with a σ^2 value too large for two ligands at a short distance. Attempts to include a shell of ligands at a distance longer than 2.15 Å were unsuccessful. Thus, the first coordination sphere of $\{Fe^{2+}\}PAH^T[]$ consists of one ligand at 1.97 Å and five ligands at an average distance of 2.14 Å. The EXAFS data required three additional components to fit the outer shell carbon single and multiple scattering from the histidine and glutamate ligands of $\{Fe^{2+}\}$-$PAH^T[]$. The single-scattering contribution from the five glutamate and histidine α-carbons was fit at 3.08 Å, while the single scattering from the four distant β-carbon and nitrogen atoms of the histidine rings was fit at 4.05 Å. Finally, the multiple scattering from the distant histidine atoms was fit at 4.36 Å.

Fits to the $\{Fe^{2+}\}PAH^R[L\text{-}Phe,5\text{-}deaza\text{-}6\text{-}MPH_4]$ EXAFS data were restricted to a total coordination number of five in accordance with the pre-edge analysis (vida supra) and MCD data (*33*). A fit to the EXAFS data with a single contribution of five nitrogen atoms at an average of 2.07 Å results in a fit value of 0.267 and a σ^2 value of 0.00964 (Table 2, fit 4). As for $\{Fe^{2+}\}PAH^T[]$, a split first coordination sphere (one ligand at 1.94 Å and four ligands at an average of 2.10 Å; Table 2, fit 5) resulted in a significantly improved fit quality, a better visual fit to the Fourier transform (Figure 4, bottom, dashed line), and more reasonable σ^2 values. Using two short (1.98 Å) and three longer ligand distances (2.12 Å) in the fit results in a larger σ^2 value for the shorter-distance, less populated shell than for the longer component (Table 2, fit 6). Attempting to fit the EXAFS data with a longer ligand (>2.15 Å) was again unsuccessful. Thus, fit 5 gives the best first-shell coordination split. As in the $\{Fe^{2+}\}PAH^T[]$ sample, three additional components were needed to fit the outer shells of the Fourier transform. The single-scattering contribution from the five histidine and glutamate α-carbons was fit at 3.07 Å, and the single scattering from the four distant β-carbon and nitrogen atoms of the histidine rings was fit at 4.02 Å. The multiple scattering from the distant histidine atoms was fit at 4.30 Å. Reducing the outer three contributions by half (Table 2, fit 7) results in exceptionally low σ^2 values for these outer shell components.

DISCUSSION

Previously existing spectroscopic information for ferrous PAH derives from CD and MCD data (*23, 33*), as well as a limited XAS study of the ferrous and substrate-only bound species (*23*). Additional pulsed EPR work has been performed for the PAH−NO adduct (*35*). The X-ray crystal structures of truncated PAH currently available (*31*) provide basic structural data; however, none of these structures are of the holoenzyme, and only one structure of the catalytically relevant ferrous form of the enzyme exists (*34*). Since the catalytically competent form of the enzyme requires protein-bound substrate and cofactor and has a ferrous active site, it is essential to the understanding of the mechanistic pathway to determine the active site structure of the ferrous ternary complex. The recently determined crystal structure of the ferrous enzyme reports four definitive iron ligands: two histidines, one monodentate glutamate, and one water molecule. Additionally, two omit densities are reported which could not be conclusively determined to be water. The reported structure of the hPheOH−Fe(II)·BH$_4$ site is six-coordinate with three waters, two histidines, and the monodentate glutamate as ligands to iron. MCD studies are sensitive to the ligand field and therefore geometry of the active site (*51*), and solution studies of the $\{Fe^{2+}\}PAH^T[]$ and $\{Fe^{2+}\}PAH^T[5\text{-}deaza\text{-}6\text{-}MPH_4]$ sites show they are spectroscopically equivalent distorted octahedral metal centers (*23, 33*). Thus, MCD indicates that no change in the iron coordination site occurs upon cofactor binding, and the two omit densities observed in the ferrous PAH crystal structure are likely disordered water sites. Therefore, by extension from the MCD studies and inference from the crystal structures, the ferrous coordination sphere is reasonably comprised of two histidines, one glutamate, and three water molecules. MCD spectroscopy has also shown the enzyme with the substrate and cofactor analogue bound to have a five-coordinate ferrous active site (*33*). The MCD data, which probe d orbital electronic structure, are here confirmed by the XAS pre-edge data, and strongly complemented by the metrical information available from XAS.

The pre-edge features of $\{Fe^{2+}\}PAH^T[]$ are similar in shape and intensity to those of six-coordinate model complexes. Additional intensity is gained through distortion from a purely octahedral site. From the EXAFS analysis, a split first coordination sphere is required (Table 2, fit 2) with the short bond significantly distorting the octahedral site, thus providing a mechanism for 4p mixing into the 3d orbitals. Alternatively, the two pre-edge features of $\{Fe^{2+}\}PAH^R$-[L-Phe,5-deaza-6-MPH$_4$] are similar in shape and intensity to those of five-coordinate model complexes. The loss of a ligand strongly eliminates the approximate inversion symmetry, which promotes 4p$_z$ mixing into the 3d$_{z^2}$ orbital, and greatly increases the pre-edge intensity.

EXAFS provides insight into the nature of the ligand lost in $\{Fe^{2+}\}PAH^R$[L-Phe,5-deaza-6-MPH$_4$] relative to $\{Fe^{2+}\}$-PAH^T[]. It is reasonable to assume that the shortest ligand in the 2.0 Å resolution structure, glutamate, at 2.1 Å will remain a short ligand distance upon reduction from ferric to ferrous iron. It could be argued that bound hydroxide could be found at <2.0 Å; however, the pK_a of H_2O bound to Fe(II) is ~9 (*52*), and would therefore likely protonate at pH 7, producing a longer Fe−O distance of 2.12 Å (*53, 54*). From these considerations, it seems reasonable to assume that the ~1.95 Å contribution in $\{Fe^{2+}\}PAH^T[]$ and $\{Fe^{2+}\}$-PAH^R[L-Phe,5-deaza-6-MPH$_4$] can be assigned to the glutamate ligand. The short Fe−ligand distance is clearly required in the fits to both $\{Fe^{2+}\}PAH^T[]$ and $\{Fe^{2+}\}PAH^R$-[L-Phe,5-deaza-6-MPH$_4$]; therefore, it is concluded that the glutamate ligand has not dissociated. If a histidine were to dissociate, there would be half the number of outer shell carbon contributions and these should be reduced in the fit concurrent with the reduction from a five- to a four-coordinate contribution at ~2.12 Å. This was tested with the results given in fit 7 in Table 2. The σ^2 values for the outer contributions were significantly reduced. In fact, the σ^2 value for the outermost contribution, the multiple scattering of the then one remaining histidine, is far lower (0.00052) than that for even the tightly bound glutamate (0.00266) at a much shorter distance, which is clearly unreasonable. Furthermore, no dramatic change is observed in a visual comparison of the carbon-based outer shell components in the Fourier transforms of both species ($R \geq$ 2.25 Å, Figure 4); peak intensities do not differ by a factor of 2, and peak positions are nearly identical. The Fourier transform peak intensities therefore lack the characteristics expected in the distant single-scattering and multiple-scattering components if loss of one histidine ligand had occurred. It should be noted that if glutamate were to dissociate the outer shell contributions would be reduced to a lesser extent. The resolution of the data is not sufficient to exclude this possibility from multiple scattering and distant shell single scattering alone. However, since the presence of the short distance in the EXAFS fit requires the glutamate ligand to remain coordinated, loss of one of the water ligands must then be responsible for the reduced coordination number upon substrate and cofactor binding. The only change that would be associated with loss of water at the active site would be a reduction in the coordination number of the first-shell component at ~2.14 Å. Fit 5 in Table 2 represents this

solution and is the best fit to the data for $\{Fe^{2+}\}PAH^R$-[L-Phe,5-deaza-6-MPH$_4$]. Thus, we can associate the six-coordinate to five-coordinate conversion of $\{Fe^{2+}\}PAH^T[]$ to $\{Fe^{2+}\}PAH^R$[L-Phe,5-deaza-6-MPH$_4$] with loss of a water at the iron active site.

It is of interest to consider the molecular mechanism of water loss as neither cosubstrate binds directly to the Fe(II). In the mononuclear non-heme iron dioxygenases DAOCS, CS1, and IPNS, a structural motif has been observed in which the uncomplexed carboxylate oxygen of the monodentate iron ligand is hydrogen bonded to a water molecule bound to the iron center. It has been suggested that the binding of substrate can perturb the conformation of the monodentate glutamate ligand, disrupting the hydrogen bond and weakening the iron−water interaction (*55*). A similar arrangement is observed in the recent hPheOH−Fe(II)·BH$_4$ crystal structure where the water trans to His285 (Wat1) is hydrogen bound to Glu330.[2] Furthermore, from an NMR modeling study, the β- and γ-protons of the Glu330 ligand have an intermolecular NOE interaction with the ring protons of the L-Phe substrate (*56*). Thus, binding of substrate must be in the proximity of the monodentate glutamate ligand and could perturb the internal hydrogen bonding of Glu330 to Wat1. It is interesting to note that this water molecule is absent from the five-coordinate ferric crystal structure of tyrosine hydroxylase with 7,8-dihydrobiopterin (2TOH) (*29*), suggesting some lability for this ligand. The loss of a water opens an iron coordination position in the proximity of the cosubstrate necessary for oxygen atom transfer to the pterin. It is thus reasonable to correlate the water trans to His285 as the ligand lost upon binding of both cosubstrates to the protein.

In summary, we have used X-ray absorption spectroscopy to acquire geometrical information regarding the ferrous active site of the resting and the substrate- and cofactor-bound forms of holo-PAH. From XAS pre-edge analysis, the resting "tense" state is six-coordinate, confirming earlier studies. EXAFS analysis fits the six-coordinate site with the short glutamate ligand at 1.97 Å and five longer contributions at an average distance of 2.14 Å. Binding of L-Phe and 5-deaza-6-MPH$_4$ causes a large increase in the pre-edge intensity, associated with 1s → 4p$_z$ character mixed into the 3d orbitals, the pattern of which is characteristic of five-coordinate ferrous complexes. This is accompanied by a shift of the EXAFS data to longer k space frequency and a decrease in the Fourier transform intensity. Fitting of the five-coordinate $\{Fe^{2+}\}PAH^R$[L-Phe,5-deaza-6-MPH$_4$] EXAFS data requires the presence of one short ligand at 1.97 Å as in the six-coordinate resting ferrous PAH, again assigned as glutamate. Removal of carbon single- and multiple-scattering contributions modeling loss of a histidine results in unreasonable σ^2 values. Thus, XAS demonstrates that water is lost from the ferrous active site of PAH when both the substrate and cofactor are bound to the enzyme. The loss of this water ligand opens a coordination position on the iron(II) center in the presence of both substrates for the reaction with O_2 to generate an active intermediate for the direct, coupled hydroxylation of the cosubstrates.

REFERENCES

1. Feig, A. L., and Lippard, S. J. (1994) *Chem. Rev. 94*, 759−805.

---

[2] Note the structure in ref *34* has Glu330 rotated relative to the structure in Figure 1.

2. Que, L., Jr., and Ho, R. Y. N. (1996) *Chem. Rev. 96*, 2607−2624.

3. Kappock, T. J., and Caradonna, J. P. (1996) *Chem. Rev. 96*, 2659−2756.

4. Shiman, R. (1985) in *Chemistry and Biochemistry of Pterins* (Blakley, R. L., and Benkovic, S. J., Eds.) pp 179−249, John Wiley & Sons, New York.

5. Kaufman, S. (1993) *Adv. Enzymol. Relat. Areas Mol. Biol. 67*, 77−264.

6. Fitzpatrick, P. F. (1991) *Biochemistry 30*, 6386−6391.

7. Goodwill, K. E., Sabatier, C., Marks, C., Raag, R., Fitzpatrick, P. F., and Stevens, R. C. (1997) *Nat. Struct. Biol. 4*, 578−585.

8. Kaufman, S., and Kaufman, E. E. (1985) in *Chemistry and Biochemistry of Pterins* (Blakley, R. L., and Benkovic, S. J., Eds.) pp 251−352, John Wiley & Sons, New York.

9. Kuhn, D. M., Ruskin, B., and Lovenberg, W. (1980) *J. Biol. Chem. 255*, 4137−4143.

10. Scriver, C. R., Eisensmith, R. C., Woo, S. L. C., and Kaufman, S. (1994) *Annu. Rev. Genet. 28*, 141−165.

11. Shiman, R., and Gray, D. W. (1980) *J. Biol. Chem. 255*, 4793−4800.

12. Kaufman, S. (1971) *Adv. Enzymol. 35*, 245−319.

13. Fisher, D. B., Kirkwood, R., and Kaufman, S. J. (1972) *J. Biol. Chem. 247*, 5161−5167.

14. Gottschall, D. W., Dietrich, R. F., Benkovic, S. J., and Shiman, R. (1982) *J. Biol. Chem. 257*, 845−849.

15. Dix, T. A., Bollag, G. E., Domanico, P. L., and Benkovic, S. J. (1985) *Biochemistry 24*, 2955−2958.

16. Døskeland, A. P., Døskeland, S. O., Øgreid, D., and Flatmark, T. (1984) *J. Biol. Chem. 259*, 11242−11248.

17. Shiman, R., Jones, S. H., and Gray, D. W. (1990) *J. Biol. Chem. 265*, 11633−11642.

18. Shiman, R., Gray, D. W., and Pater, A. (1979) *J. Biol. Chem. 254*, 11300−11306.

19. Hill, M. A., Marota, J. J. A., and Shiman, R. (1988) *J. Biol. Chem. 263*, 5646−5655.

20. Marota, J. J. A., and Shiman, R. (1984) *Biochemistry 23*, 1303−1311.

21. Wallick, D. E., Bloom, L. M., Gaffney, B. J., and Benkovic, S. J. (1984) *Biochemistry 23*, 1295−1302.

22. Shiman, R. (1980) *J. Biol. Chem. 255*, 10029−10032.

23. Loeb, K. E., Westre, T. E., Kappock, T. J., Mitic, N., Glasfeld, E., Caradonna, J. P., Hedman, B., Hodgson, K. O., and Solomon, E. I. (1997) *J. Am. Chem. Soc. 119*, 1901−1915.

24. Shiman, R., Xia, T., Hill, M. A., and Gray, D. W. (1994) *J. Biol. Chem. 269*, 24647−24656.

25. Bloom, M. L., Benkovic, S. J., and Gaffney, B. J. (1986) *Biochemistry 25*, 4204−4210.

26. Erlandsen, H., Bjørgo, E., Flatmark, T., and Stevens, R. C. (2000) *Biochemistry 39*, 2208−2217.

27. Kobe, B., Jennings, I. G., House, C. M., Michell, B. J., Goodwill, K. E., Santarsiero, B. D., Stevens, R. C., Cotton, R. G. H., and Kemp, B. E. (1999) *Nat. Struct. Biol. 6*, 442−448.

28. Flatmark, T., and Stevens, R. C. (1999) *Chem. Rev. 99*, 2137−2160.

29. Goodwill, K. E., Sabatier, C., and Stevens, R. C. (1998) *Biochemistry 37*, 13437−13445.

30. Gibbs, B. S., Wojchowski, D., and Benkovic, S. J. (1993) *J. Biol. Chem. 268*, 8046−8052.

31. Erlandsen, H., Fusetti, F., Martínez, A., Hough, E., Flatmark, T., and Stevens, R. C. (1997) *Nat. Struct. Biol. 4*, 995−1000.

32. Shiman, R., Gray, D. W., and Hill, M. A. (1994) *J. Biol. Chem. 269*, 24637−24646.

33. Kemsley, J. N., Mitic, N., Zaleski, K. L., Caradonna, J. P., and Solomon, E. I. (1999) *J. Am. Chem. Soc. 121*, 1528−1536.

34. Andersen, O. A., Flatmark, T., and Hough, E. (2001) *J. Mol. Biol. 314*, 279−291.

35. Wang, W. U., Mitić, N., Caradonna, J., and Peisach, J. (1999) *FASEB J. 13*, A1499.

36. Brown, C. A., Pavlosky, M. A., Westre, T. E., Zhang, Y., Hedman, B., Hodgson, K. O., and Solomon, E. I. (1995) *J. Am. Chem. Soc. 117*, 715−732.

37. Moad, G., Luthy, C. L., Benkovic, P. A., and Benkovic, S. J. (1979) *J. Am. Chem. Soc. 101*, 6068−6076.

38. Breitmaier, E., and Gassenmann, S. (1971) *Chem. Ber. 104*, 665−667.

39. Stark, E., and Breitmaier, E. (1973) *Tetrahedron 29*, 2209−2217.

40. Scott, R. A., Hahn, J. E., Doniach, S., Freeman, H. C., and Hodgson, K. O. (1982) *J. Am. Chem. Soc. 104*, 5364−5369.

41. Cramer, S. P., Tench, O., Yochum, M., and George, G. N. (1988) *Nucl. Instrum. Methods Phys. Rev. A266*, 586−591.

42. DeWitt, J. G., Bentsen, J. G., Rosenzweig, A. C., Hedman, B., Green, J., Pilkington, S., Papaefthymiou, G. C., Dalton, H., Hodgson, K. O., and Lippard, S. J. (1991) *J. Am. Chem. Soc. 113*, 9219−9235.

43. Cramer, S. P., and Hodgson, K. O. (1979) *Prog. Inorg. Chem. 25*, 1−39.

44. Scott, R. A. (1985) *Methods Enzymol. 117*, 414−459.

45. Zhang, H. H., Hedman, B., and Hodgson, K. O. (1999) in *Inorganic Electronic Structure and Spectroscopy* (Solomon, E. I., and Lever, A. B. P., Eds.) pp 513−554, John Wiley & Sons, New York.

46. George, G. N. (2001) *EDG_FIT*, Stanford Synchrotron Radiation Laboratory, Stanford Linear Accelerator Center, Stanford University, Stanford, CA.

47. Randall, C. R., Shu, L., Chiou, Y.-M., Hagen, K. S., Ito, M., Kitajima, N., Lachicotte, R. J., Zang, Y., and Que, L., Jr. (1995) *Inorg. Chem. 34*, 1036−1039.

48. Westre, T. E., Kennepohl, P., DeWitt, J. G., Hedman, B., Hodgson, K. O., and Solomon, E. I. (1997) *J. Am. Chem. Soc. 119*, 6297−6314.

49. Shu, L., Chiou, Y.-M., Orville, A. M., Miller, M. A., Lipscomb, J. D., and Que, L., Jr. (1995) *Biochemistry 34*, 6649−6659.

50. Davis, M. I., Wasinger, E. C., Westre, T. E., Zaleski, J. M., Orville, A. M., Lipscomb, J. D., Hedman, B., Hodgson, K. O., and Solomon, E. I. (1999) *Inorg. Chem. 38*, 3676−3683.

51. Pavel, E. G., Kitajima, N., and Solomon, E. I. (1998) *J. Am. Chem. Soc. 120*, 3949−3962.

52. Baes, C. F., Jr., and Mesmer, R. E. (1984) in *The Hydrolysis of Cations*, Chapters 10, 12, and 13, John Wiley & Sons, New York.

53. Strouse, J., Layten, S. W., and Strouse, C. E. (1977) *J. Am. Chem. Soc. 99*, 562−572.

54. Do, J., Wang, X., and Jacobson, A. J. (1999) *J. Solid State Chem. 143*, 77−85.

55. Zhou, J., Kelly, W. L., Bachman, B. O., Gunsior, M., Townsend, C. A., and Solomon, E. I. (2001) *J. Am. Chem. Soc. 123*, 7388−7398.

56. Teigen, K., Frøystein, N. Å., and Martínez, A. (1999) *J. Mol. Biol. 294*, 807−823.

57. Waisbren, S. E. (1999) *Ment. Retard. Dev. Dis. Res. Rev. 5*, 125−131.